Check for updates

Received: 26 November 2021 | Revised: 17 March 2022 | Accepted: 18 May 2022 | Published on: 20 June 2022

DOI: 10.1002/gamm.202200014

ORIGINAL PAPER

Applicability of correlated digital image correlation and infrared thermography for measuring mesomechanical deformation in foams and auxetics

Sergej Grednev[1] | Stefan Bronder[1] | Francesco Kunz[1] | Martin Reis[1] | Susanne-Marie Kirsch[2] | Felix Welsch[2] | Stefan Seelecke[2] | Stefan Diebels[1] | Anne Jung[1]

[1]Applied Mechanics, Saarland University, Saarbrücken, Germany

[2]Intelligent Material Systems Lab, Saarland University, Saarbrücken, Germany

Correspondence
Anne Jung, Applied Mechanics, Saarland University, Campus C6.3, 66123 Saarbrücken, Germany.
Email: anne.jung@mx.uni-saarland.de

Abstract

Cellular materials such as metal foams or auxetic metamaterials are interesting microheterogeneous materials used for lightweight construction and as energy absorbers. Their macroscopic behavior is related to their specific mesoscopic deformation by a strong structure-property-relationship. Digital image correlation and infrared thermography are two methods to visualize and study the local deformation behavior in materials. The present study deals with the full-field thermomechanical analysis of the mesomechanical deformation in Ni/PU hybrid foams and Ni/polymer hybrid auxetic structures performing a correlative digital image correlation and infrared thermography. Instead of comparing and correlating only the primary output variables of both methods, strain and temperature, also strain rates and temperature rates occurring during deformation were compared. These allow for a better correlation and more conclusive results than obtained using only the primary output variables.

KEYWORDS

auxetic, digital image correlation, foam, thermography

1 | INTRODUCTION

Today's engineering work requires an increased amount of lightweight constructions and material efficiency. Cellular materials such as foams or three dimensional (3D) auxetics are bioinspired materials mimicking the blueprints of nature [67]. They combine high stiffness with a low density in addition to a plateau stress over a large deformation regime, making them ideal for applications in lightweight constructions or as crash absorbers [28]. There exists a broad spectrum of open cell and closed cell foams producible from for example, polymers or metals. Open cell foams consist of a base material with a stochastic distribution of interconnected pores [24]. Hybrid foams are created by applying a coating, for instance via electrochemistry, offering enhanced mechanical properties, compared to a conventional metal foam. Those hybrid foams were studied by different research groups in recent years. Boonyongmaneerat et al. [8] produced a NiW/Al hybrid foam and studied the mechanical properties under uniaxial compression. Bouwhuis et al. [9] and Jung

This is an open access article under the terms of the Creative Commons Attribution-NonCommercial-NoDerivs License, which permits use and distribution in any medium, provided the original work is properly cited, the use is non-commercial and no modifications or adaptations are made.
© 2022 The Authors. *GAMM - Mitteilungen* published by Wiley-VCH GmbH.

15222608, 2022, 3-4, Downloaded from https://onlinelibrary.wiley.com/doi/10.1002/gamm.202200014 by Universitaet Des Saarlandes, Wiley Online Library on [18/10/2022]. See the Terms and Conditions (https://onlinelibrary.wiley.com/terms-and-conditions) on Wiley Online Library for rules of use; OA articles are governed by the applicable Creative Commons License

et al. [37] produced and investigated the energy absorption capacity properties of Ni/Al hybrid foams. Jung et al. [38-40] and Jung and Diebels [34,35] further studied the mechanical behavior from the macro down to the atomic scale for Ni/Al hybrid foams for uni- and multiaxial loading. Sun et al. [72] investigated Al/Cu foams both in finite element (FE) simulations as well as experimentally. Numerical simulations on single struts revealed that the main contribution to the mechanical properties results from the coating [33]. Hence, a new economic process was developed by Jung and Diebels [33] to synthesize a Ni/PU hybrid foam with a light and cheap polyurethane (PU) substrate foam. Bronder et al. [13] adopted this procedure to coat an auxetic polymer structure with nickel and subjected those specimens to quasi-static and dynamic experiments. Furthermore, they removed the PU core via pyrolysis to create even lighter and more ductile hollow structures.

3D auxetics with their superior impact and indentation resistance [2] and fracture toughness [48] are suitable for applications in ballistic and blast protection [26,57,58] or crash absorbers [7,66]. They derive their main property, the negative Poisson's ratio, from their microstructure and were first artificially produced and experimentally investigated by Lakes et al. [47]. Hence, the specific mesomechanical deformation is the key for the negative Poisson's ratio. Due to the application in dynamic scenarios, many investigations concerning the dynamic loading case were done in recent years [30,53,59]. For more information on auxetic materials the reader is referred to the literature [49,50].

For a better understanding of the deformation process, an investigation with digital image correlation (DIC) is often beneficial. Therefore, Adorna et al. [1] compared different DIC tools. DIC in general visualizes local strain fields and thereby helps to understand the mesomechanical deformation with a sub-pixel accuracy for example, in a failure investigation on the surface of a specimen [61]. The basic principal of DIC is taking pictures during loading of the specimen and tracking the motion of image points through an unique gray-scale pattern. Then, the pattern before and after the loading step is compared, resulting in a local displacement and rotation field. More detailed information on the DIC process can be found in [18,19,61,73,76]. The deformation behavior of foams on the mesoscale was mainly studied by strain mapping on the foam surface using DIC [4,5,80,81] and by X-ray computed tomography [3,27,32]. Most of the investigations in the past haven been performed on closed cell metal foams. Thornton and Magree [74] were, in 1975, among the first to investigate the deformation behavior of closed cell aluminum foams under uniaxial compression. By taking pictures of the surface during the deformation, they concluded the main deformation mechanism to be the buckling of the cell walls throughout the entire loading. In contrast to all later investigations, Thornton and Magree stated the buckling was uniformly distributed over the entire specimen. Bart-Smith et al. [3] were the first ones to use DIC on the entire foam surface to study the deformation behavior on the mesoscale. Hereby, the foam structure is directly usable as speckle pattern, since it is a stochastic structure. Bart-Smith et al. [3] found that the foams deformed heterogeneously, even well before reaching the plastic collapse stress (PCS), by forming deformation bands with the size of approximately one cell diameter. The initiation and propagation of new deformation bands succeeds in the overall deformation of the sample. X-ray tomography further revealed a strong influence of the mechanical properties by morphological defects or inhomogeneous density distribution. In their investigation of open cell foams, Bart-Smith et al. [3] found a homogeneous deformation, which was only related to the PCS peak. In addition, they concluded the pore shape to be of much more importance to the deformation during the PCS and plateau phase than the pore size. Bastawros et al. [4-6] used surface strain mapping to investigate the deformation mechanism on cell- or pore-level of closed cell and open cell aluminum foams, proposing three stages of deformation up to the valley stress after the PCS peak. Zhou et al. [80,81] adopted these stages and expanded the strain range up to 0.3, hereby identifying plastic bending as the dominating deformation and failure mechanism under compression loading.

However, DIC is only capable of mapping the local surface motion and X-ray tomography with high spatial resolution is impractical for large specimens [19]. During the deformation process, elastic and plastic deformation causes energy dissipation in the material resulting in a temperature distribution in the specimen's volume and hence a change in surface temperature [64]. To gain more understanding of the processes in the specimen's volume infrared thermography (IRT) is a suitable method as shown in [41]. Generally, IRT enables contactless determination of an entire two-dimensional surface, exploiting that a body above 0 K emits infrared radiation. As a boundary technique, IRT is not only capable of detecting temperatures on the surface, but also in a limited depth inside a semi-transparent specimen [51]. In experiments without vacuum the convective heat transfer to the surrounding fluid in for example, air has to be considered. This behavior can also be used to characterize the material parameters like heat transfer coefficient, heat conductivity and latent heats, as shown in [55,56,79]. Additional applications in material science are the characterization of shape memory alloys [20,43,65,68], the failure analysis of components and structures [10] or the plastic deformation detection [62]. Starting from the 90's [70], in the last few years IRT became of rising interest also in industrial applications [60], especially because of its non-destructive and non-invasive testing qualities for example, damage detection in composites [16,51,54].

15222608, 2022, 3-4, Downloaded from https://onlinelibrary.wiley.com/doi/10.1002/gamm.202200014 by Universitaet Des Saarlandes, Wiley Online Library on [18/10/2022]. See the Terms and Conditions (https://onlinelibrary.wiley.com/terms-and-conditions) on Wiley Online Library for rules of use; OA articles are governed by the applicable Creative Commons License

Further applications are in pollution monitoring or medicine [54]. More detailed information on the theory of IRT can be found in [52,78].

The main applications of IRT related to foams nowadays are the monitoring of the exothermic foaming process of closed cell foams [71] and the exothermic reaction in open cell foam catalysts [29]. On the topic of cellular metals, recently Duarte et al. [25] gave an overview of the characterization techniques. As mentioned above, in the last few years the interest on foams has increased which is also visible by the amount of different scientific investigations using IRT in for example, specific applications like energy absorption [46] and crush performance [23] or mechanical analysis [14,22,63,77]. Recently, also fatigue life investigations are supported by IRT [75].

DIC and IRT are both capable of studying the local surface behavior by full-field measurement of different physical properties [45,69]. Since the 90's the combined determination of mechanical and thermal parameters has been established in science [25,65,69], also in foams [42]. Nevertheless, both methods have advantages and disadvantages, resulting from their different measurement principles [54,61]. For simple 2D-DIC, only an inexpensive optical camera and the application of a random speckle pattern [21] on the specimen surface are necessary. If there is already an intrinsic pattern due to the specimen structure, this pattern can be used and no additional specimen preparation is needed. Hence, the natural microstructure of foams can be used directly as speckle pattern, but the resolution of observable features in DIC are than restricted to the pore size. If a better resolution is needed, there should also be the application of an additional speckle pattern onto the foam structure. Because DIC accuracy is strongly linked to the strain per frame, the image resolution is of high importance and a good specimen illumination is necessary. Therefore, it is superior for quasi-static experiments and will need a more expensive equipment when going to dynamic deformation velocities [45]. In comparison, the camera system for IRT is more expensive due to the required high spatial, temporal, and thermal resolution. To gain a thermal resolution in the single digit mK range, semiconductor sensors (InSb) exploiting the inner photo effect are used and cooled below 80 K, resulting in a more complex system. Additionally, the specimen's surface emissivity has to be known. Therefore, the surface is usually coated with special IRT lacquer. To suppress infrared reflections from surrounding objects an emissivity of the surface near one is ideal. The IRT system captures, comparable to optical cameras, the intensity of the incoming infrared light which is a measure for the specimen surface temperature. High recording rates enable precise local detection of the smallest heat sources or sinks due to the negligible diffusion effects by thermal conductivity. In contrast to DIC, the IRT reflects directly, without correlation of two images, the surface temperature of the specimen, hence IRT exhibits no fundamental upper limitation on the strain rate. Since the infrared radiation of the specimen is measured, no external illumination is necessary even under dynamic loading [54].

In combining DIC and IRT it becomes possible to overcome the disadvantages of both methods and gain more information on the deformation and failure process. The first comparison of DIC and IRT was done by Chrysochoose et al. [17] on quasi-static tensile experiments with IR camera and CCD camera on opposing sides. They were able to derive the local energy balance and show the influence of dissipated and thermomechanical coupling mechanisms on the stress/strain behavior through a thermodynamic analysis. Later, a more detailed comparison of both methods was done by Krstulović-Opara et al. [45] on aluminum specimens from dynamic down to quasi-static loading. Their conclusion was that the heat generated by plastic deformation processes is comparable to the plastic strain and hence, IRT and DIC are both suitable investigation methods. In 2016 Cholewa et al. [15] calibrated a system for 3D-DIC, coupled with IR imaging, to compensate for differences in camera resolution. They evaluated different lacquers and investigated E-glass/vinyl and ester/balsa sandwich composites from one side under compression loading and simultaneous heating. Jung et al. [41] were the first to investigate metal foams with a full-field thermography. The study was done on open cell aluminum and Ni/Al hybrid foams at different strain rates in the quasi-static regime, resulting in deviations between temperature field and strain field. The largest strains in DIC did not always correspond to the hottest areas measured by IRT. This is a result of cooling and heat transfer of the specimens. While DIC offers the entire strain history, IRT shows only the current deformation as heat increase, which vanishes due to heat transfer to the pistons of the test rig and cooling in air. This effect is more pronounced with reduced strain rates. Those results were in contradiction to the results of Krstulović-Opara et al. [45]. However, Jung et al. [41] found IRT images to present the places of concentrated plastic deformation, while DIC images give the complete strain history. Due to cooling caused by heat convection and conduction, the hottest areas only present the current plastic deformation zones. Jung et al. [42] further directly compared IRT with DIC images, allowing a direct coupling of local strain fields with local temperature fields. Through that, the evolution of the energy absorption capacity can be expressed as a function of the strain rate. They further concluded Ni hollow strut foams to be better energy absorbers than Ni/PU or CuNi/PU hybrid foams.

The present contribution focuses on the full-field thermomechanical analysis of the local mesoscale deformation on Ni/PU hybrid foams of different porosity and modified Ni/polymer hybrid auxetics using coupled DIC and IRT. Different

15222608, 2022, 3-4, Downloaded from https://onlinelibrary.wiley.com/doi/10.1002/gamm.202200014 by Universitaet Des Saarlandes, Wiley Online Library on [18/10/2022]. See the Terms and Conditions (https://onlinelibrary.wiley.com/terms-and-conditions) on Wiley Online Library for rules of use; OA articles are governed by the applicable Creative Commons License

material compositions and geometries are compared regarding their crush and thermal behavior during deformation. In contrast to the state of the art, this contribution compares not only the local strain field from DIC with the local temperature field from IRT but also the corresponding local strain rates and local temperature rates to gain an enhanced understanding of underlying deformation mechanisms. To ease the correlation of both methods, a fully automated software tool was developed which compares the results of DIC and IRT at same deformation state. The tool calculates the strain rates and temperature rates, as well as the temperature increase for the specimens as function of the global strain. The computationally efficient software tool allows a quick analysis of large data sets to support the evaluation of numerous experiments and hence to gain a deeper understanding of the local deformation in cellular materials.

2 | MATERIALS AND METHODS

2.1 | Ni/PU hybrid foams and hybrid auxetics

Hybrid auxetic structures and Ni/PU hybrid foams were investigated in this study. The modified auxetic structures used in the experiments are similar to the ones investigated by Bronder et al. [12]. In accordance to their full factorial testing plan, the specimen with all geometry parameters at minimum level (strut thickness 0.5 mm, waist 0.5 mm, size 7 mm) was chosen for manufacturing to achieve good coating results. The unit cell is supplemented with an additional half strut in the middle (Figure 1A) to increase stability after an initial deformation [11]. The template structure of the modified auxetic geometry was 3D printed using the stereolithographic (SLA) system (Phrozen mini 4K, Phrozen, Taiwan). The auxetic structures were layer-wise build by exposing a photosensitive resin (Phrozen Aqua-Gray 4K resin, Phrozen, Taiwan) to a high-resoluted, monochrome 4k LED screen. The achievable resolution is approximately 35 µm. After the basic structure was produced, it was rinsed with isopropanol and irradiated for 300 s from all sides in a UV chamber with a rotating base plate. Thereby, the resin was fully cured and the structure was stable enough for the subsequent treatment.

The commercial precursors for the two different hybrid foams (Schaumstoff Direkt Rüdiger Nolte, Enger, Germany) had a pore size of approximately 10 ppi and 20 ppi (pores per inch), respectively and were cut into a cylindrical form with a diameter of 210 mm and a thickness of 40 mm by hot wire cutting.

The electrodeposition of a nickel coating on the two different polymeric template structures (foams or auxetic structure) made an electrically conductive surface necessary. Therefore, the templates were pre-coated with a thin layer of carbon lacquer (Graphit 33, CRC Kontakt Chemie, Iffezheim, Germany) in a dip-coating process for two times and dried with pressured air for 10 min. For the coating process, a commercial nickelsulfamate electrolyte (Enthone GmbH, Langenfeld, Germany) with a nickel concentration of 110 g L^{-1} was used. The reaction was performed at a temperature of 50°C and a pH of 3.8. The specimens were coated with an average coating thickness of 120 µm using a direct current of 1.3 mA cm^{-2}.

The 3D-printed geometries were coated in a special anode-cathode configuration developed by Jung et al. [36] due to their small geometry of 24.2 mm × 24.2 mm × 34.2 mm. The anode consists of a double-walled hollow cube, built with titanium expanded metal that is filled with nickel pellets (A.M.P.E.R.E. GmbH, Dietzenbach, Germany). The geometry was

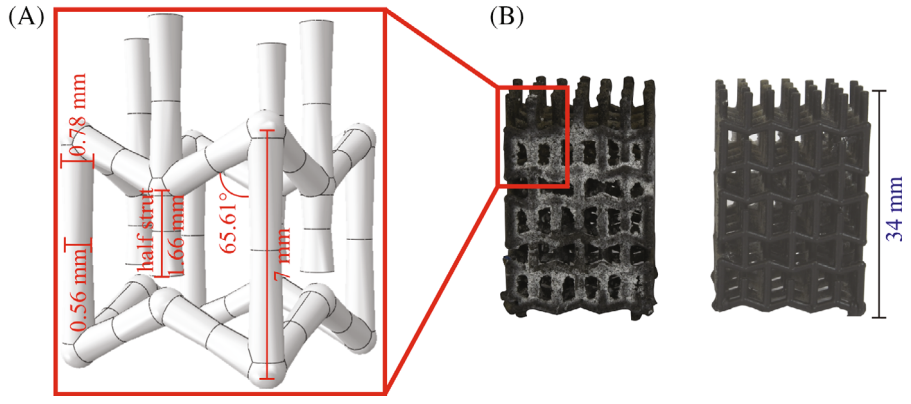

FIGURE 1 (A) Modified auxetic unit cell with added half strut; (B) coated auxetic specimen for compression experiments with UV fluorescent speckle pattern (left) and low emission lacquer (right)

15222608, 2022, 3-4, Downloaded from https://onlinelibrary.wiley.com/doi/10.1002/gamm.202200014 by Universitaet Des Saarlandes, Wiley Online Library on [18/10/2022]. See the Terms and Conditions (https://onlinelibrary.wiley.com/terms-and-conditions) on Wiley Online Library for rules of use; OA articles are governed by the applicable Creative Commons License

TABLE 1 Densities of the different specimen types

Specimen type	Density (g/cm^3)
10 ppi hybrid foams	0.321 ± 0.021
20 ppi hybrid foams	0.399 ± 0.019
Modified hybrid auxetics	0.466 ± 0.060

placed in the center of the cage-like anode to ensure a maximum concentration of nickel ions produced by the sacrificial anode.

The Ni/PU hybrid foam was produced in a flow-controlled electrodeposition cell with two anodes, one above and one below the cathode [31]. The disc-like foam specimen had a diameter of 210 mm and a height of 40 mm. During the deposition process, the ion concentration was kept at a maximum level by dissolving the two sacrificial anodes. A constant circulated flow of filtered and temperated electrolyte through the foam ensures an exchange and the removal of impurities.

After the deposition, both hybrid structures were rinsed in water and dried. The Ni/PU hybrid foam specimens were extracted out of the bigger foam plate with a band saw in a comparable geometry to the 3D printed auxetic specimen. The densities of the foams and auxetic structures are shown in Table 1.

2.2 | Uniaxial compression experiments

The universal testing machine ElectroPuls E10000 (Ltd. Instron, Pfungstand, Germany) with a strain rate of 0.18 s^{-1} and a 10 kN force sensor was used for the uniaxial compression experiments. For some statistics three to four samples of each specimen type were studied. All specimens were sprayed with black varnish having a thermal emissivity coefficient of 0.97 (no. 105202, TETENAL Europe GmbH, Norderstedt, Germany) for the thermal imaging on one side. The coating was applied on the observed surface as thin as possible, to avoid influences of the thermal time constant. The opposite side was primed with an ultraviolet (UV) fluorescent paint (ARASOL-109 UV Blue, ARALON COLOR GmbH, Heiligenroth, Deutschland) and a black speckle pattern was applied by spray can (Dupli-Color RAL 9005 Acryl Spray, Motip Dupli GmbH, Hassmersheim, Germany) (see Figure 2 for the digital image correlation (DIC) (Figure 1B)). Consequently, the experiments were recorded with an infrared (IR) camera system (ImageIR9360, Infratec GmbH, Dresden, Germany) on one side and a 9 Megapixel charged coupled device (CCD) camera (Manta G-917B, Allied Visions Technologies GmbH, Puchheim, Germany) on the other side (Figure 3). The applied UV-DIC according to König et al. [44] improves not only the quality of the DIC measurements but also improves the IRT results measured on the opposite side by avoiding reflections of visible light. The whole setup was covered with a black box to minimize environmental influences and supports a dull and dark environment without light reflections. On the side of the CCD camera, UV light (LDL-130X15UV365, CCS Inc., Brüssel, Belgien) was used to illuminate the specimen and an IR filter glass was put in between to minimize thermal radiation influences from the CCD camera in order to achieve better results with the IR imaging. Both cameras were connected to the machine trigger and took pictures with 20 frames per second (fps), so one picture per 0.9% global strain. To reach a continuous loading of the specimen, the trigger of the universal testing machine only starts and stops the image acquisition with a rising and falling edge. While the rising edge the IR camera starts shooting with the previously set frame rate. The CCD camera is triggered by the trigger out of the IR system. The DIC evaluation was done using the software ISTRA4D® (Dantec Dynamics, Skovlunde, Denmark). Two successive images were matched and the displacement was accumulated with a facet size of 55 px and a grid spacing of 20 px. It was not only used to visualize local engineering strain but also to reliable calculate the global engineering strain instead of using machine stroke. The IR system is able to capture the local time resolved temperature evolution on the specimen surface with a resolution of 25 mK and a measurement accuracy of +/−1 K. The combination of the 1280×1024 px, sensor and the 50 mm lens with a close-up, supports a pixel size of 60 µm. The experiment configuration and the evaluation was done using the software IRBIS®.

2.3 | Automatic tool for full-field thermomechanical analysis

To automatically compare and further study the data received from DIC and IRT analysis, a Python™ tool was developed. It allows to directly compare DIC and IRT images, showing the same state of deformation, along with the corresponding

15222608, 2022, 3-4, Downloaded from https://onlinelibrary.wiley.com/doi/10.1002/gamm.202200014 by Universitaet Des Saarlandes, Wiley Online Library on [18/10/2022]. See the Terms and Conditions (https://onlinelibrary.wiley.com/terms-and-conditions) on Wiley Online Library for rules of use; OA articles are governed by the applicable Creative Commons License

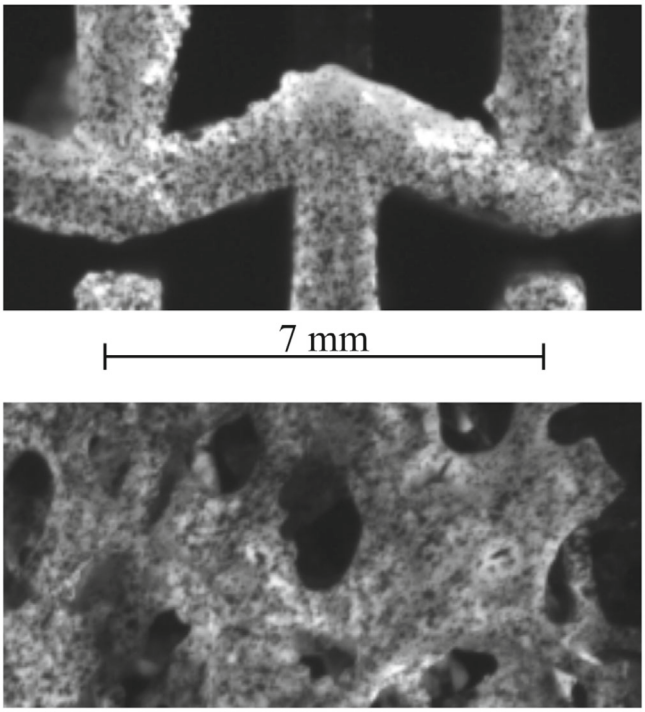

FIGURE 2 Zoomed in view of the CCD camera of the speckle pattern, auxetic structure (top), foam (bottom) with equal scale bar.

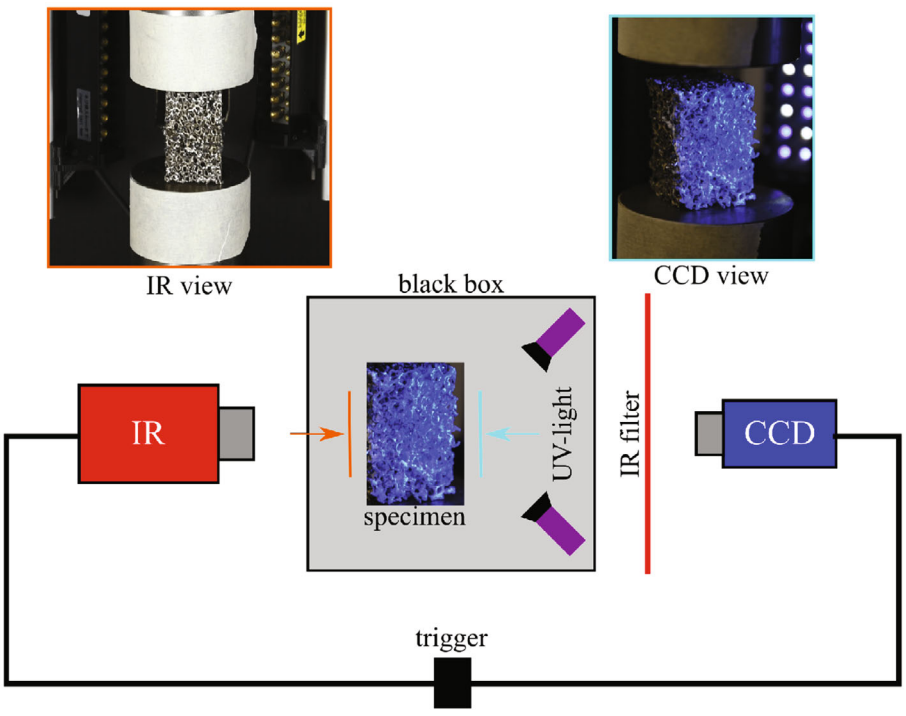

FIGURE 3 Experimental setup of the compression tests.

15222608, 2022, 3-4, Downloaded from https://onlinelibrary.wiley.com/doi/10.1002/gamm.202200014 by Universitaet Des Saarlandes, Wiley Online Library on [18/10/2022]. See the Terms and Conditions (https://onlinelibrary.wiley.com/terms-and-conditions) on Wiley Online Library for rules of use; OA articles are governed by the applicable Creative Commons License

strain rates and temperature rates, which are calculated by a subroutine within the tool. Furthermore, it allows to draw an arbitrary number of vertical lines into DIC and IRT images as well as the corresponding rate images, and create line plots depicting the respective quantities along these lines.

As input, the tool expects the results of the DIC analysis for each step of deformation, that is, taken image, where only the horizontal and vertical positions within the foam with corresponding local strains are needed, and the IRT matrices for each step of deformation. Since the CCD camera and IR camera were simultaneously triggered and used the same frame rate of 20 frames per second, DIC and IRT images at the same position within the sequence of images show the same state of deformation.

The main user input consists of the desired number of images, which will be uniformly spaced to cover the whole range of global deformation and the desired number of lines per image, which will be uniformly spaced to cover the whole width of the respective image. The Python™ tool is divided into four major parts, preprocessing, DIC part, IRT part, and postprocessing.

As a part of the preprocessing, first the relevant data from ISTRA4D® output files is extracted. The relevant data consists of the x and y coordinates of the points used for DIC analysis, together with corresponding local strains at these points. For each image the height of the foam is determined as the difference of maximum and minimum coordinate values of the vertical axis. By comparing the height of the foam in each image with the unloaded state, the global strain for each image is calculated. Depending on user input, a number of image indices is selected to provide an equidistant spacing of global strains for the whole loading process. It should be noted that only meaningful results from DIC analysis are used. When DIC matching fails, it fails completely, including all following steps. Those steps are discarded before feeding the data to the tool.

The main task of the DIC part is to interpolate the local strain values onto a regular grid. This is necessary because the points provided by ISTRA4D® are not regularly spaced. On the one hand this impedes the plotting process, since many matplotlib® functions expect the data points to be evenly spaced and on the other hand, and more importantly, it makes the creation of line plots virtually impossible. For the interpolation process, nearest-neighbor interpolation is used. In addition, the DIC images are mirrored along the center vertical axis to account for the fact, that the CCD camera and IRT camera were facing each other during the experiments (see Figure 3).

The primary function of the IRT part is to cut the IRT images produced by IRBIS®, so that only the specimen becomes visible, because the IRT images, by default, show both the specimen and the upper piston of the universal testing machine. Here the main challenge lies in automatically detecting the border between specimen and piston in every image. The automatic border detection was facilitated by a combination of Gaussian filters and the Canny edge detection algorithm. Additionally, to provide more insight into the deformation process, a plot, depicting the increase in maximum temperature over global strain, is created.

Once the DIC and IRT images are available in appropriate form, in both parts the following steps are executed. The strain rates and temperature rates are calculated as the slope of the secant between the respective chosen image and a prior reference image. By taking into account the known and constant frame rate of the cameras, the difference in image index can be directly translated into a time difference between images. Here, an image index distance of 10 was chosen, that is, a time difference of 0.5 s. Data for the line plots is produced by extracting the respective quantities (strains, temperatures, and corresponding rates) along certain coordinates from the matrices. These coordinates are automatically determined in accordance with user input. Extracting this data enables the tool to produce line plots of the respective quantity versus relative vertical position.

In the final part, all intermediate data produced so far is combined, transformed where needed, and put into context, in a way that facilitates straightforward interpretation. An overview of the structure and functionalities of the automatic correlation tool is shown in Figure 4.

3 | RESULTS AND DISCUSSION

3.1 | Stress–strain response of the different specimen types

The engineering stress–strain diagrams of the two different hybrid foams and the modified hybrid auxetic structure are shown in Figure 5. They outline the global strain, which is defined for the entire specimen length, while later local strain results from the DIC for specific positions in the specimens. The 20 ppi foams provide higher plastic collapse stress (PCS) values than the 10 ppi foams. Both foams outline a distinct hardening during compression which can be traced back to

15222608, 2022, 3-4, Downloaded from https://onlinelibrary.wiley.com/doi/10.1002/gamm.202200014 by Universitaet Des Saarlandes, Wiley Online Library on [18/10/2022]. See the Terms and Conditions (https://onlinelibrary.wiley.com/terms-and-conditions) on Wiley Online Library for rules of use; OA articles are governed by the applicable Creative Commons License

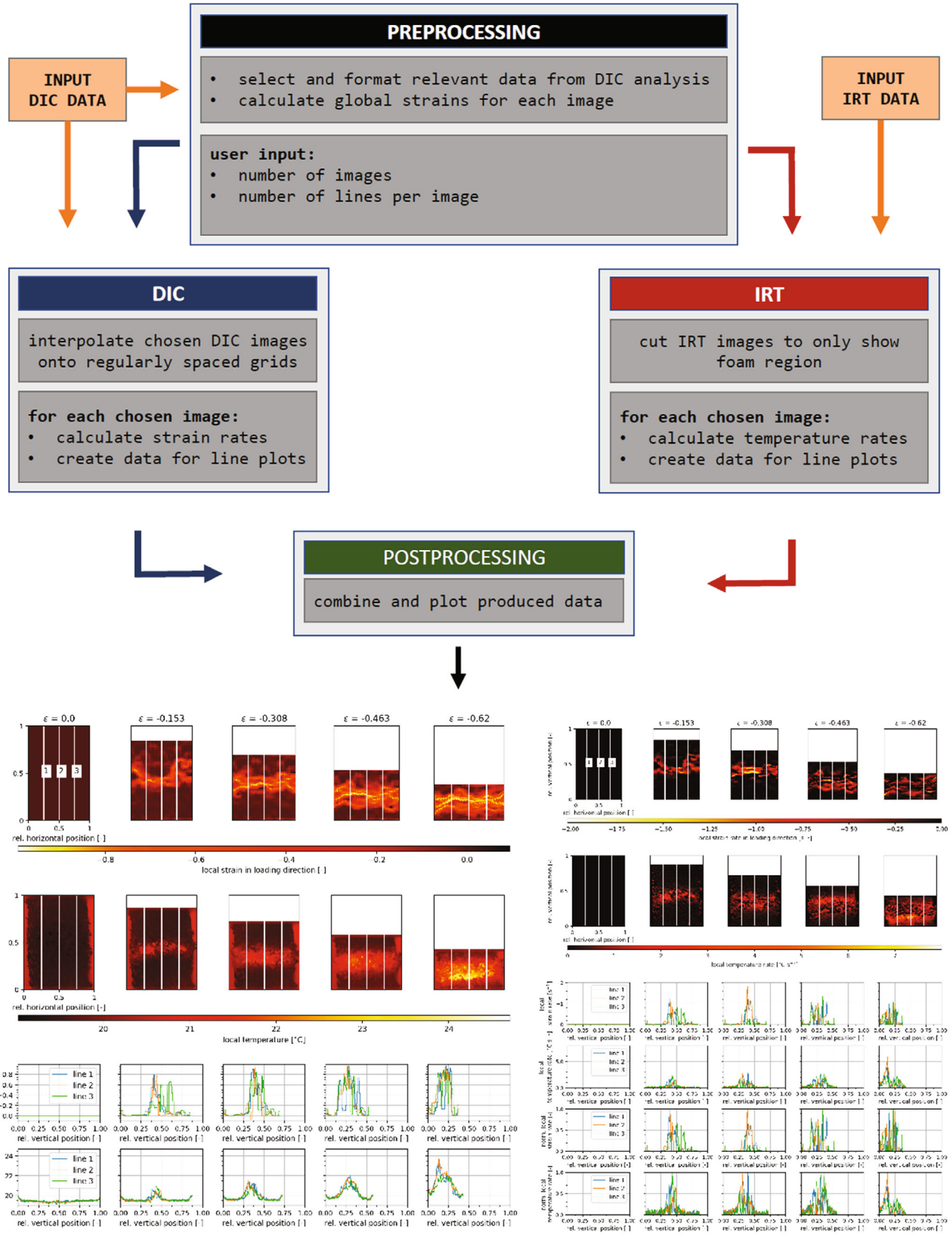

FIGURE 4 Structure and functionalities of the automatic correlation tool for thermomechanical analysis of deformation. A detailed, larger view of the individual output pictures is given later in the Section 3.

15222608, 2022, 3-4, Downloaded from https://onlinelibrary.wiley.com/doi/10.1002/gamm.202200014 by Universitaet Des Saarlandes, Wiley Online Library on [18/10/2022]. See the Terms and Conditions (https://onlinelibrary.wiley.com/terms-and-conditions) on Wiley Online Library for rules of use; OA articles are governed by the applicable Creative Commons License

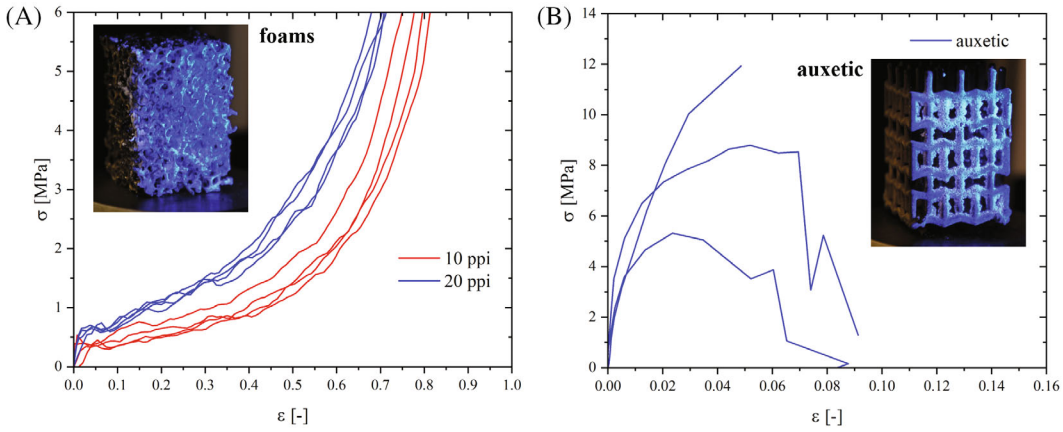

FIGURE 5 Stress–strain diagrams of (A) 10 ppi and 20 ppi foams, (B) of modified auxetic structures including a representative image of the specimens under UV light

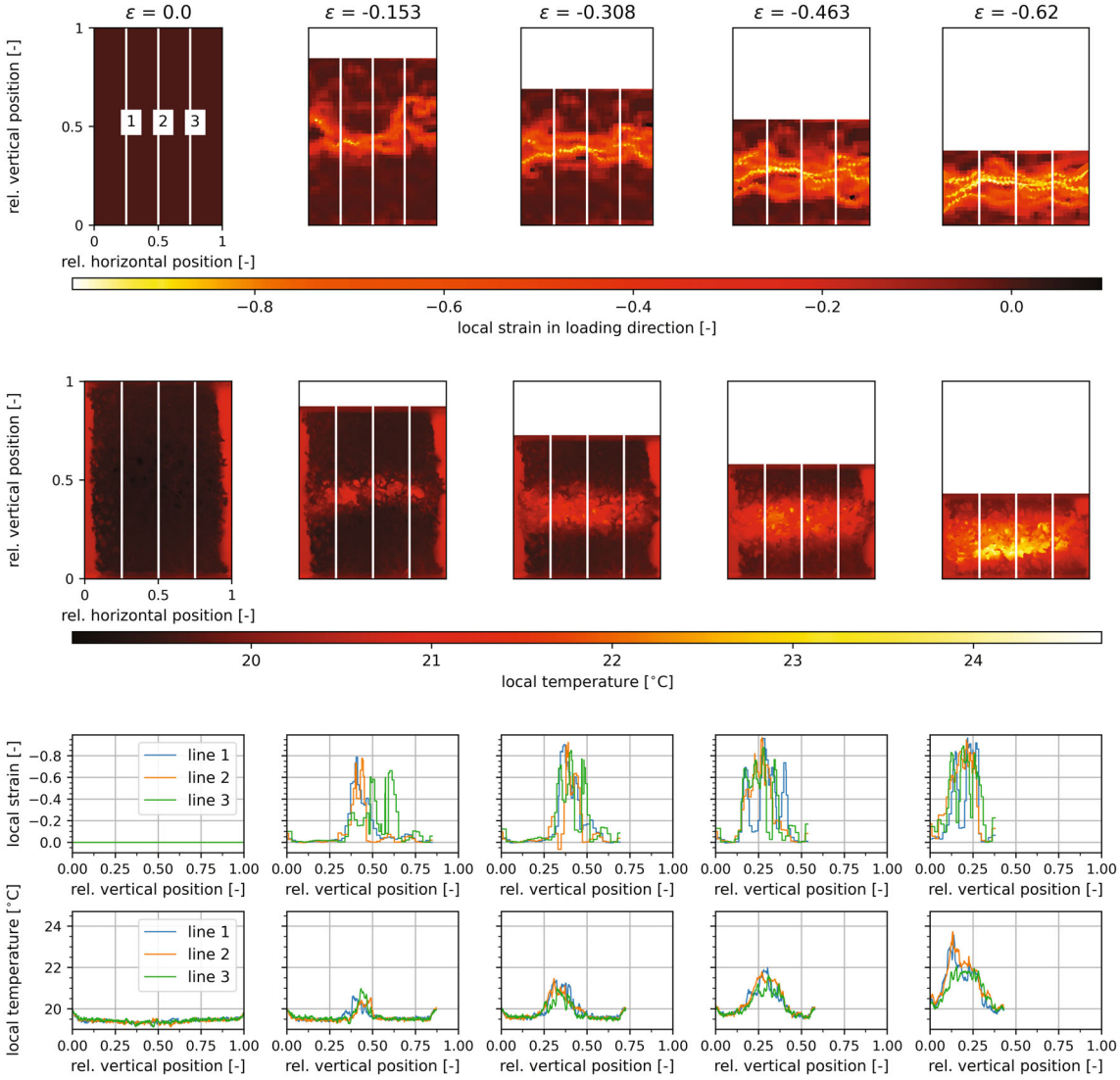

FIGURE 6 Exemplary 10 ppi hybrid foam: local strain fields (first row) and local temperature fields (second row) for different global strain states including the line plots for local strain (third row) and local temperature (fourth row) for three positions (see white lines) in the foam.

15222608, 2022, 3-4, Downloaded from https://onlinelibrary.wiley.com/doi/10.1002/gamm.202200014 by Universitaet Des Saarlandes, Wiley Online Library on [18/10/2022]. See the Terms and Conditions (https://onlinelibrary.wiley.com/terms-and-conditions) on Wiley Online Library for rules of use; OA articles are governed by the applicable Creative Commons License

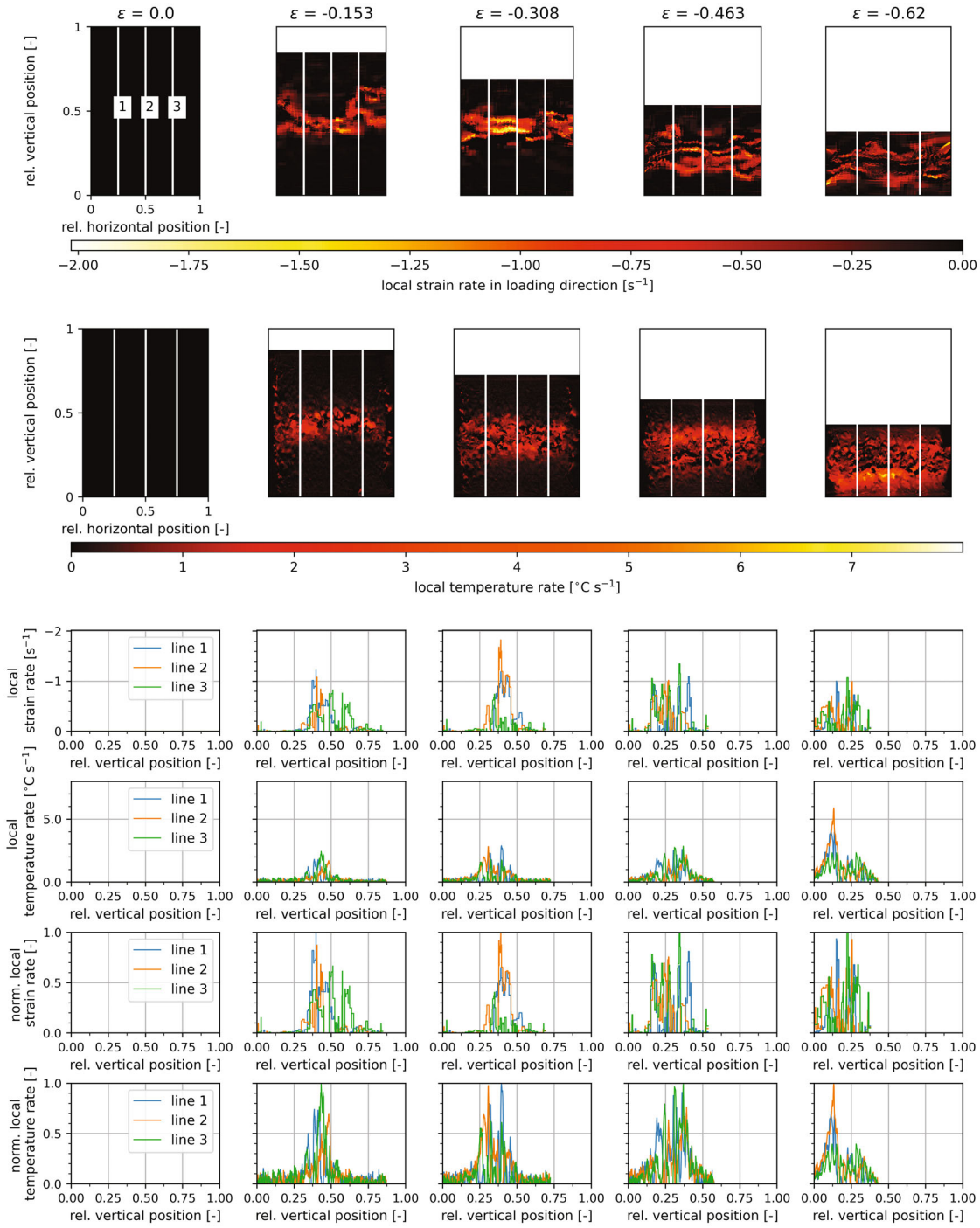

FIGURE 7 Exemplary 10 ppi hybrid foam: local strain rate fields (first row) and local temperature rate fields (second row) for different global strain states including the line plots for local strain rates (third row) and local temperature rates (fourth row) for three positions (see white lines) in the foam. For better comparison, the line plots of the normalized local strain rate (fifth row) and local temperature rate (sixth row) are also shown.

slight inhomogeneities in the coating thickness distribution with lower coating thicknesses in the center of the foams. Pore layers with lower coating thickness collapse first successively followed by pore layers with increasing coating thickness. Hence, there is not a constant plateau stress, but an increasing plateau region. The auxetic structures have a much higher PCS than the foams. While the foams have a PCS of about 0.5 to 0.75 MPa, the auxetics provide 5 to 12 MPa. However, there is a large scattering for the auxetics. This is a result of the high brittleness of the auxetic structures also resulting in very low fracture strains of less than 0.10.

15222608, 2022, 3-4, Downloaded from https://onlinelibrary.wiley.com/doi/10.1002/gamm.202200014 by Universitaet Des Saarlandes, Wiley Online Library on [18/10/2022]. See the Terms and Conditions (https://onlinelibrary.wiley.com/terms-and-conditions) on Wiley Online Library for rules of use; OA articles are governed by the applicable Creative Commons License

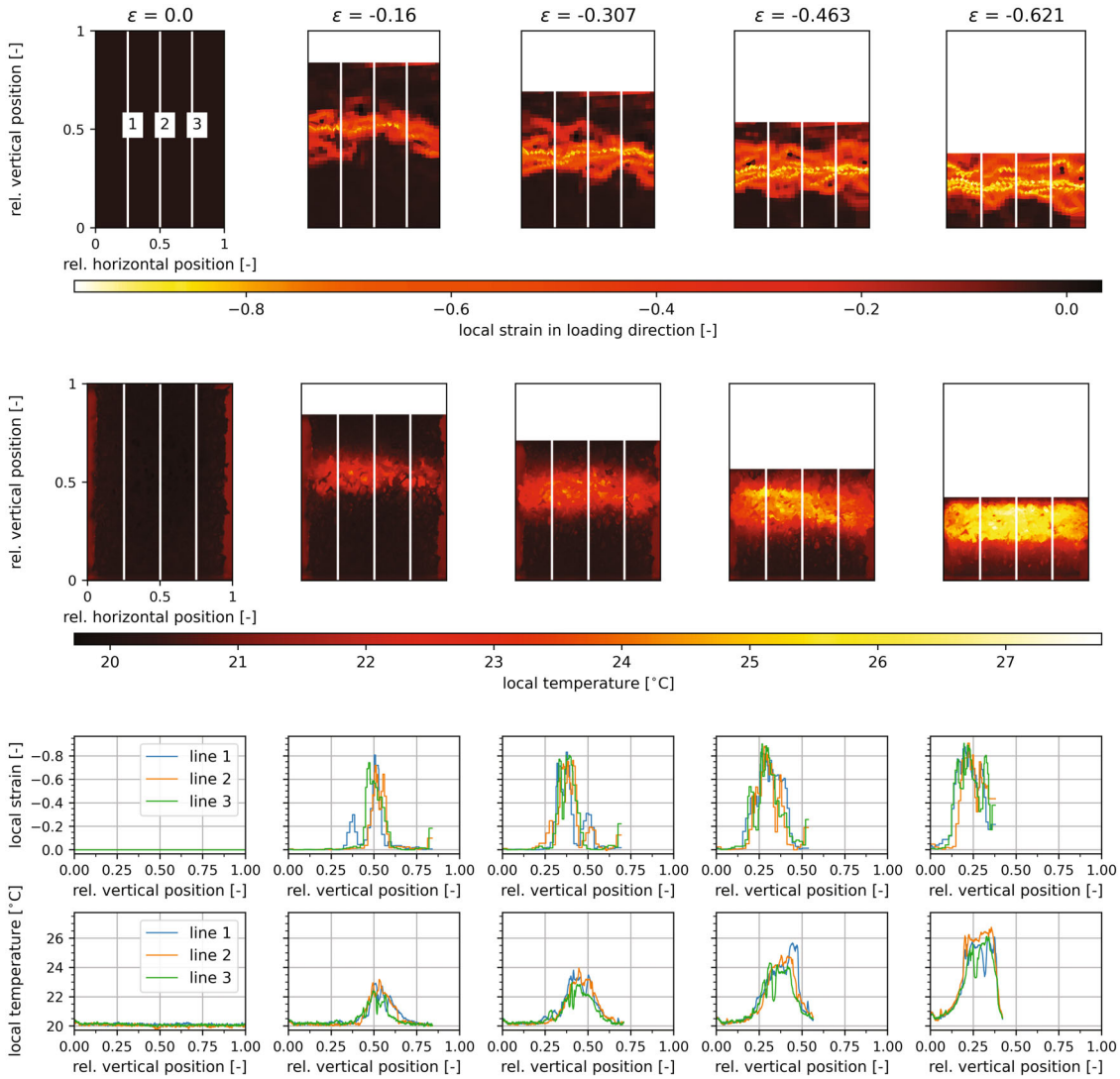

FIGURE 8 Exemplary 20 ppi hybrid foam: local strain fields (first row) and local temperature fields (second row) for different global strain states including the line plots for local strain (third row) and local temperature (fourth row) for three positions (see white lines) in the foam.

3.2 | Fully-coupled thermomechanical analysis of foams

Usually, correlative DIC and IRT means there is a direct correlation of the primary output variables of both methods, strain and temperature. Hence, the local strain fields and temperature fields of a representative 10 ppi foam specimen are shown in Figure 6 including line plots on three positions of the foam outlining the local strain and local temperature for these three positions. The line plots represent the local variables for three vertical lines in the foam parallel to loading direction (see white lines in Figure 6). The scales of both local fields are shown in similar color for a better comparison of the strain fields and temperature fields. Since increasing compression strain results in more negative strain values but also in more positive temperature values, the scales are inverted.

The images of the fields show only some similarities. The entire deformation zone is of equal size, however, highest temperatures are not at same position as highest strains. From the line plots, local strains as well as local temperatures reflect the width of the deformation band in the specific field variable. The strain bands are broader than the temperature bands.

Since DIC uses the undeformed state as reference image for all further deformation states, it outlines the entire deformation history, while IRT shows the current deformation zones especially for non-dynamic deformations, where the

15222608, 2022, 3-4, Downloaded from https://onlinelibrary.wiley.com/doi/10.1002/gamm.202200014 by Universitaet Des Saarlandes, Wiley Online Library on [18/10/2022]. See the Terms and Conditions (https://onlinelibrary.wiley.com/terms-and-conditions) on Wiley Online Library for rules of use; OA articles are governed by the applicable Creative Commons License

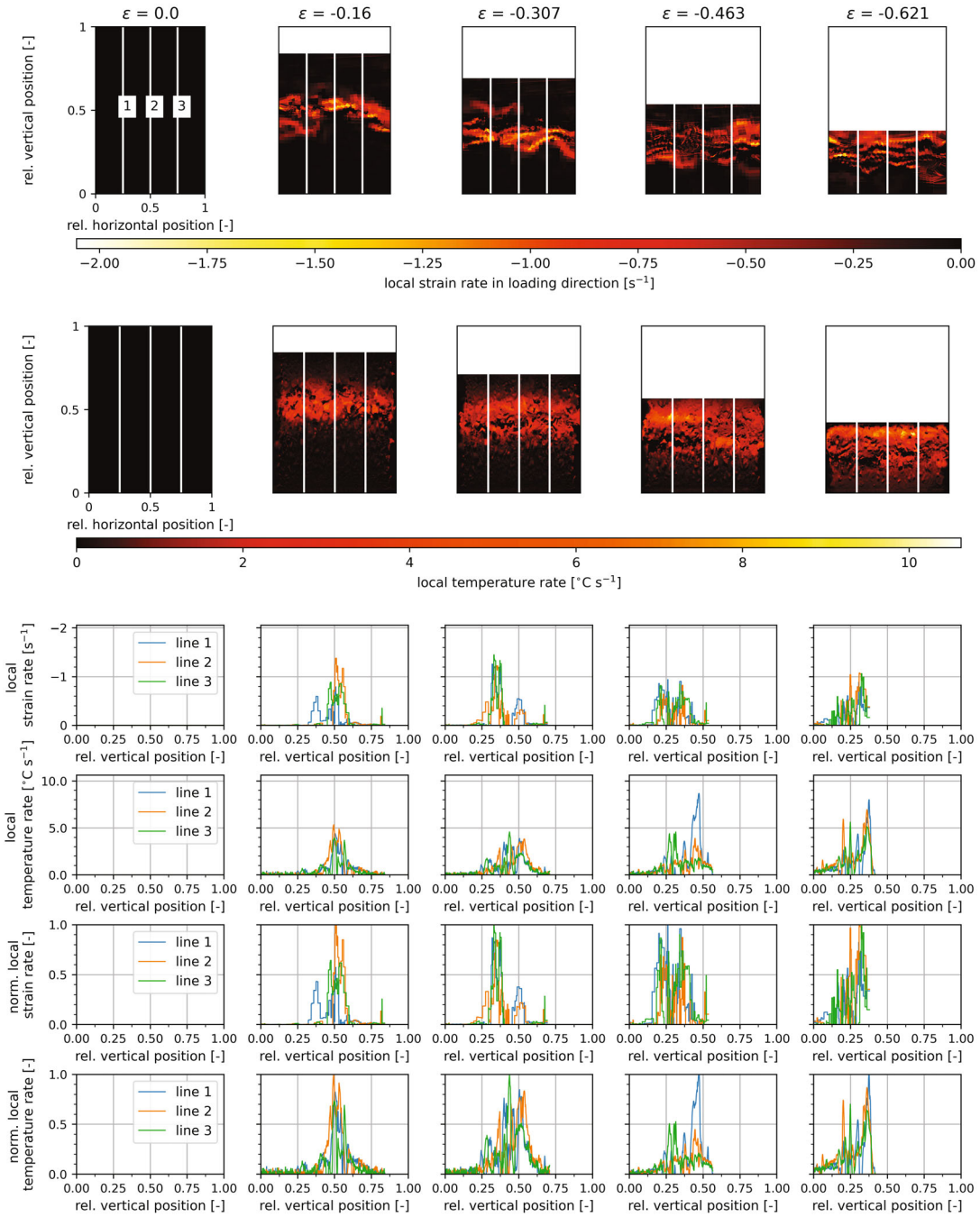

FIGURE 9 Exemplary 20 ppi hybrid foam: local strain rate fields (first row) and local temperature rate fields (second row) for different global strain states including the line plots for local strain rates (third row) and local temperature rates (fourth row) for three positions (see white lines) in the foam. For better comparison, the line plots of the normalized local strain rate (fifth row) and local temperature rate (sixth row) are also shown.

specimen is able to partially cool down during further deformation. Therefore, Figure 7 compares not the local strains and local temperatures but the local rates of both primary variables. The local strain rates present the change in strain at a specific position in the foam during deformation while the local temperature rate is defined as the change in temperature at a specific position. Hence, both rates show only the changes in the field variables from one deformation state to another state which results in the response of the specific field variable caused only by this part of the entire deformation history. The strain rate images consist of much sharper deformation bands than the temperature rate images resulting from heat loss during deformation due to heat conduction and heat convection in the specimens to the air and to the loading plates of

15222608, 2022, 3-4, Downloaded from https://onlinelibrary.wiley.com/doi/10.1002/gamm.202200014 by Universitaet Des Saarlandes, Wiley Online Library on [18/10/2022]. See the Terms and Conditions (https://onlinelibrary.wiley.com/terms-and-conditions) on Wiley Online Library for rules of use; OA articles are governed by the applicable Creative Commons License

the testing machine. But areas of high strain rates are areas of high temperature rates too and provide a better correlation than the strain fields and temperature fields with each other.

Since two different, independent physical quantities are compared, the best method is to normalize the rates, which is done by the maximal occurring values to a maximal normalized value of 1 (compare Figure 7 fifth and sixth row). Although the strain rate is more sensitive to small deformations, the line plots of the rates also show a much better correlation than the line plots of the primary variables (see Figure 6 third and fourth row). In most cases, high local strain rates correspond to high local temperature rates.

The same comparisons of local strain and local temperature (see Figure 8) as well as local strain rate and local temperature rate (see Figure 9) were done for the 20 ppi hybrid foams. The temperature fields show much more heat for the 20 ppi foams than for the 10 ppi foams, thereby making a local comparison of strain field and temperature field more difficult because there are less pronounced local differences (Figure 8 first and second row). The line plots are more equal than for the 10 ppi foams. Similar to the 10 ppi foams, there is a much better correlation between the local strain rate fields and the local temperature rate fields (Figure 9). Since DIC is only able to visualize surface deformations, IRT and hence the temperature fields outline the temperature not only at the outer surface of the foams but also at least partially from inside the foam structure, there cannot be a perfect match of the line plots and local fields. IRT provides partially volumetric deformation data, while DIC offers only surface deformation data which also might change in case of different observation sides such as in the setup, where DIC and IRT observe the specimens from opposite sides. However, beside some minor differences the line plots of the rates correlate quite well in shape and width. This is a proof for similar amount of deformation and similar width of the deformation bands measured by DIC and IRT.

To get a deeper understanding of the local deformation mechanism and why there is a better correlation of DIC and IRT for the 20 ppi foams than for the 10 ppi foams, a comparison of the stress–strain diagrams and the maximal increase in temperature as function of global strain is performed in Figure 10 for the 10 ppi and 20 ppi foams.

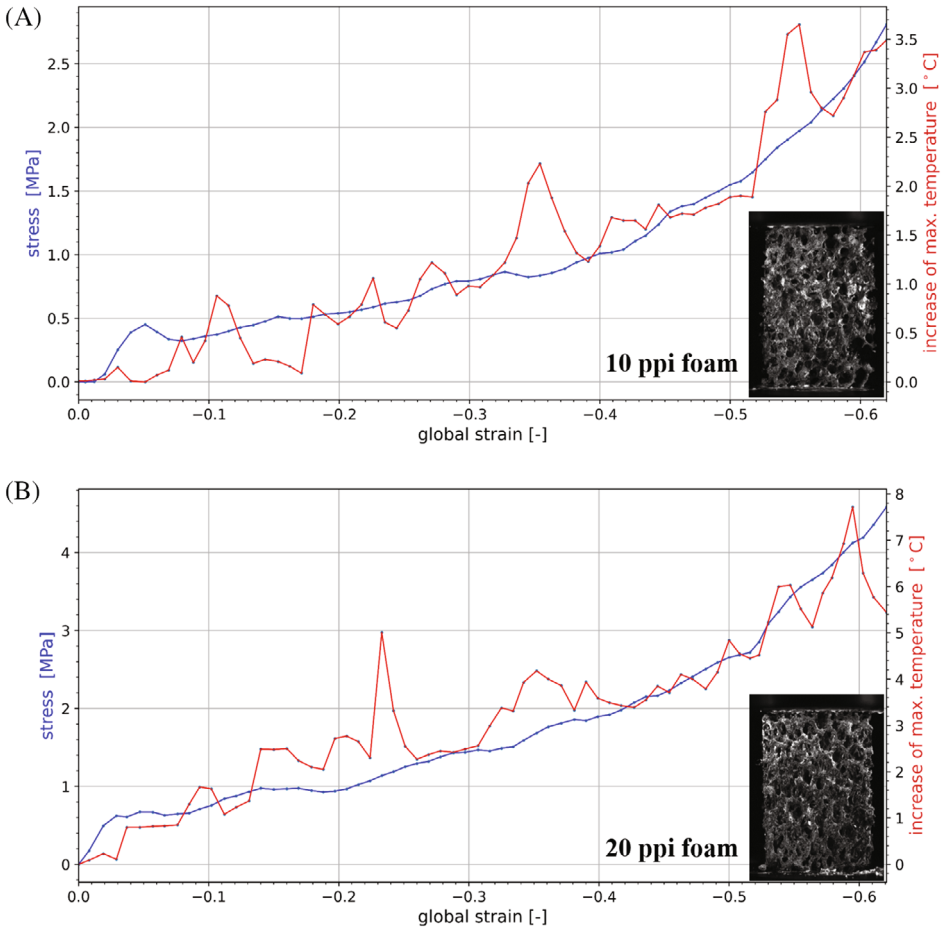

FIGURE 10 Stress–strain diagrams and increase in temperature-strain diagrams for an exemplary (A) 10 ppi and (B) 20 ppi hybrid foam

15222608, 2022, 3-4, Downloaded from https://onlinelibrary.wiley.com/doi/10.1002/gamm.202200014 by Universitaet Des Saarlandes, Wiley Online Library on [18/10/2022]. See the Terms and Conditions (https://onlinelibrary.wiley.com/terms-and-conditions) on Wiley Online Library for rules of use; OA articles are governed by the applicable Creative Commons License

With a few small local exceptions, the increase in maximal temperature as function of global strain has the same shape as the stress–strain diagram for both porosities of the hybrid foams. The 20 ppi foams do not only offer higher stresses than the 10 ppi foams but also an approximately two times higher increase in the maximal temperature during the deformation. Both phenomena are not only caused by the smaller pore size but mostly by the larger density and the higher ratio of nickel on the hybrid foams (see Table 1). The larger heat production during deformation is the key for the better correlation of DIC and IRT for the 20 ppi foams compared to the 10 ppi foams and provides a better sensitivity of the method.

3.3 | Fully-coupled thermomechanical analysis of auxetics

Previous studies already showed that it is beneficial for bulk materials as well as for foams to perform a fully-coupled thermomechanical analysis to get deeper insight in the deformation mechanism [42]. However, up to now, there was no study on the application of correlative DIC and IRT to periodic structures such as auxetics. In order to study if it is possible to gain further information on the deformation mechanism, the previously performed analysis of the hybrid foams was extended to the modified auxetic hybrid structures. Figure 11 shows the local strain fields and temperature fields as well as

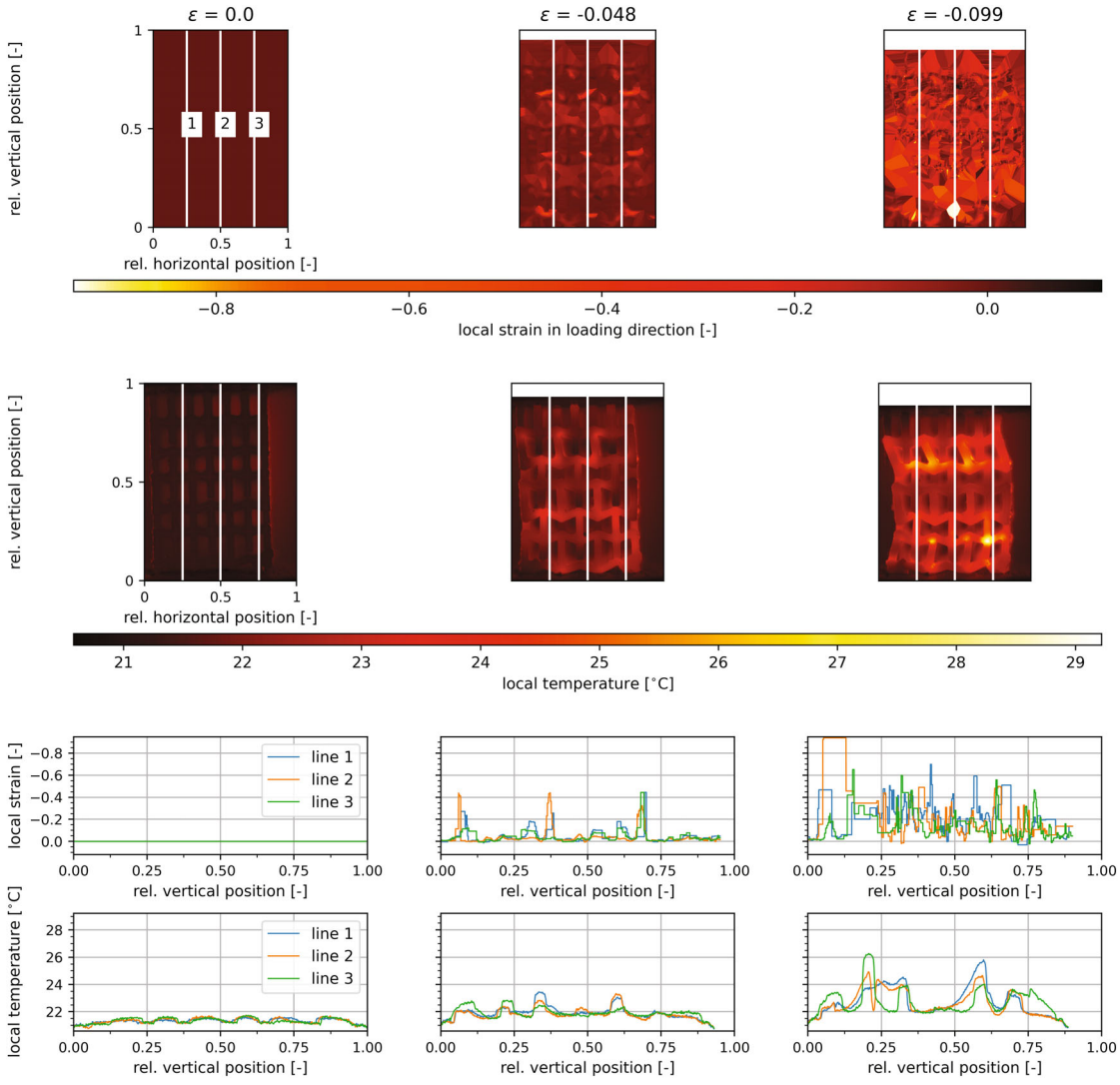

FIGURE 11 Exemplary modified hybrid auxetic structure: local strain fields (first row) and local temperature fields (second row) for different global strain states including the line plots for local strain (third row) and local temperature (fourth row) for three positions (see white lines) in the auxetic structure.

15222608, 2022, 3-4, Downloaded from https://onlinelibrary.wiley.com/doi/10.1002/gamm.202200014 by Universitaet Des Saarlandes, Wiley Online Library on [18/10/2022]. See the Terms and Conditions (https://onlinelibrary.wiley.com/terms-and-conditions) on Wiley Online Library for rules of use; OA articles are governed by the applicable Creative Commons License

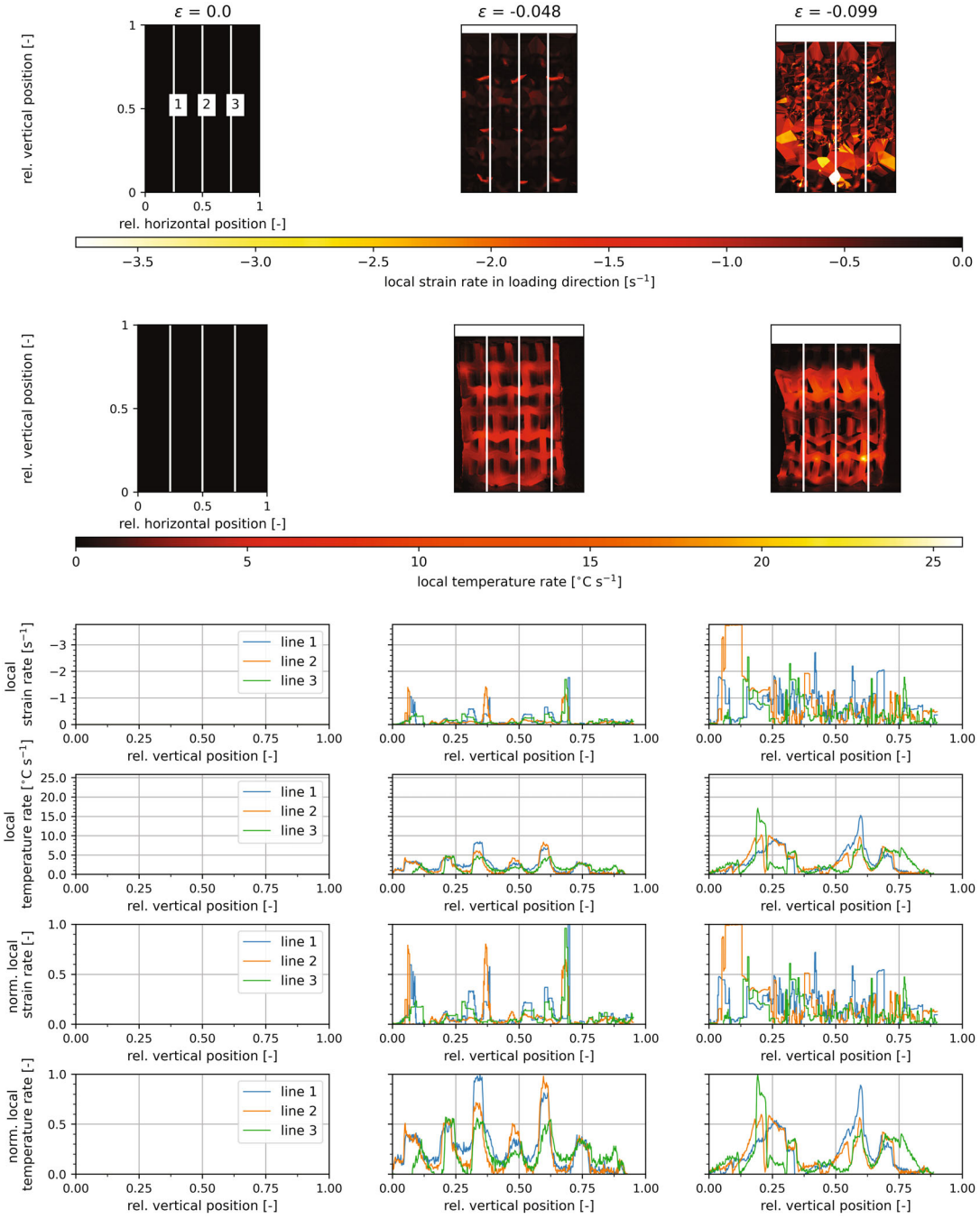

FIGURE 12 Exemplary modified hybrid auxetic structure: local strain rate fields (first row) and local temperature rate fields (second row) for different global strain states including the line plots for local strain rates (third row) and local temperature rates (fourth row) for three positions (see white lines) in the auxetic structure. For better comparison, the line plots of the normalized local strain rate (fifth row) and local temperature rate (sixth row) are also shown.

the corresponding line plots. The stress–strain diagrams in Figure 5 already outlined a very brittle deformation behavior for the auxetic structures resulting in a very small strain of fracture of about 10% or less. This sudden brittle failure causes problems in the DIC analysis, since there are too few images recorded to trace these large deformations between two images. That is why DIC failed in providing useful information for the local strain fields and the line plots. Especially for a global deformation of $\varepsilon = -0.099$ a physical interpretation of the local strain field is not possible. In contrast, IRT provides useful information on the local deformation mechanism since it directly measures the temperature and there is no need for a cross correlation or something else between the previous images. The largest deformations are in the node points at the interconnection of three struts. The upper unit cell layer starts to shear off just before the sudden brittle failure.

15222608, 2022, 3-4, Downloaded from https://onlinelibrary.wiley.com/doi/10.1002/gamm.202200014 by Universitaet Des Saarlandes, Wiley Online Library on [18/10/2022]. See the Terms and Conditions (https://onlinelibrary.wiley.com/terms-and-conditions) on Wiley Online Library for rules of use; OA articles are governed by the applicable Creative Commons License

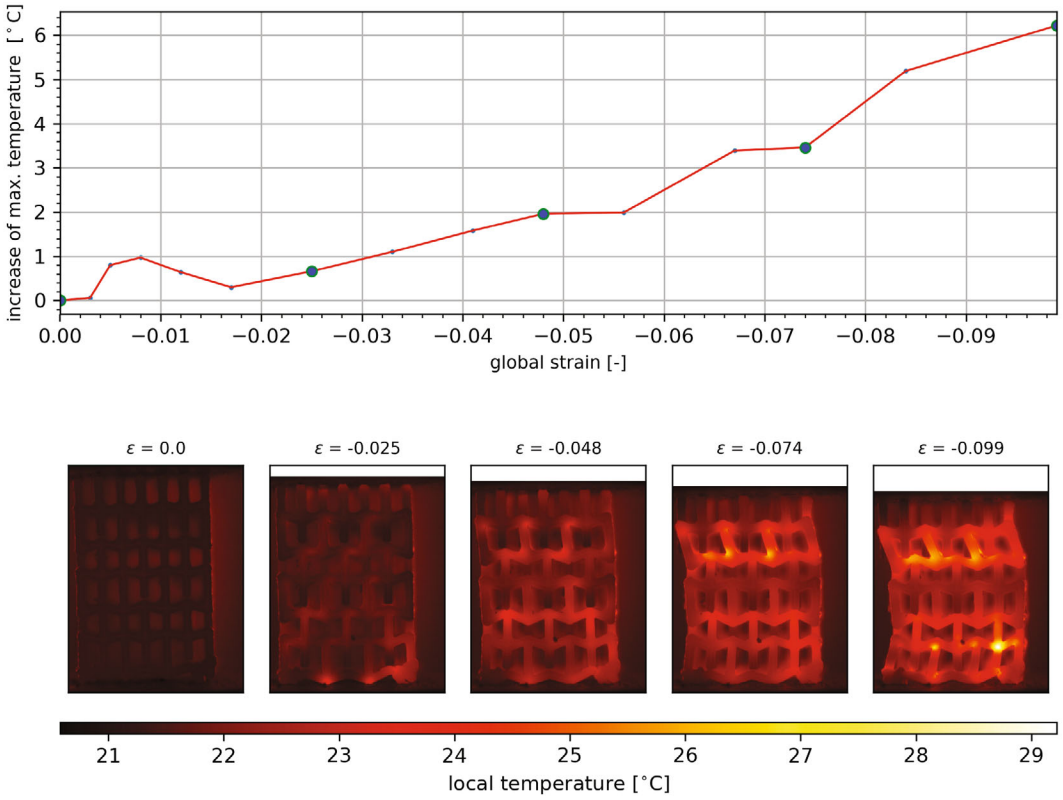

FIGURE 13 Increase of maximal temperature in auxetic structure during loading (top) and corresponding local temperature images (down).

The correlation of the local strain rates and local temperature rates (see Figure 12) provides similar findings as for the correlation between the primary local field variables of DIC and IRT (see Figure 11). However, the local temperature rate fields again improve the visualization of the current locations of largest deformation. The line plots of the normalized temperature rates clearly show the location of the largest deformation by the largest values. In contrast to the stochastic distribution of the peaks in the line plots of the foams, the periodic structure of the auxetics is also reflected in the height and width of the peaks in their line plots of the local temperature rates.

Due to the small fracture strain, a reliable comparison of the stress–strain diagram and the increase in temperature as for the hybrid foams is not possible for the auxetics. However, Figure 13 provides a further proof of principle that IRT offers useful information for the analysis of the mesomechanical deformation behavior of the auxetics. Although, the experiments were performed not under high dynamic but only under intermediate strain rates, the maximal observable temperature increases with increasing global strain, visualizing local deformations without significant errors by too large heat conduction or convection, which would for example, lead to broad diffuse peak width in the line plots (see Figure 12 sixth row). The density of the auxetic structures is larger than for the 20 ppi foams, nevertheless the maximal increase in temperature is with about 6°C a little bit lower. This might be an effect of the much larger pores in the auxetics compared to the foams. But the heat evolution is sufficient for a conclusive correlation despite of the occurring heat loss during the tests.

4 | CONCLUSIONS

The present contribution focused on the applicability of full-field thermomechanical analysis correlating the data of DIC and IRT measurements to study the local mesomechanical deformation behavior in different types of cellular materials such as stochastic Ni/PU hybrid foams of different porosity and periodic Ni/polymer hybrid auxetics. While the hybrid foams were more ductile, the hybrid auxetics displayed a sudden catastrophic failure due to a brittle material behavior. From a material point of view, future work will deal with the study of heat treatment methods to improve the ductility

15222608, 2022, 3-4, Downloaded from https://onlinelibrary.wiley.com/doi/10.1002/gamm.202200014 by Universitaet Des Saarlandes, Wiley Online Library on [18/10/2022]. See the Terms and Conditions (https://onlinelibrary.wiley.com/terms-and-conditions) on Wiley Online Library for rules of use; OA articles are governed by the applicable Creative Commons License

of the hybrid auxetics combined with a removal of the polymer template. Otherwise, an application as potential energy absorber would not be possible.

Concerning the methodical aspects, the fully-coupled thermomechanical analysis of the foams showed the huge potential of a correlated DIC and IRT analysis combining the advantages of both methods. This contribution proved for the first time that correlating rates of the primary variables of both methods, the local strain rates and local temperature rates, is much better than a direct correlation of strain and temperature. However, a meaningful analysis is only possible if there is a sufficient evolution of heat during successive deformation without a loss for example, due to heat convection and heat conduction. Hence, materials with higher densities and experiments under sufficiently high strain rates are necessary.

The sudden, brittle failure of the auxetic structures outlines the advantages and disadvantages of both methods. IRT is better for the observation of the deformation and damage behavior under fast and sudden failure such as brittle fracture. The deformation in subsequent images used for DIC must be comparably small to allow for a calculation of displacements and strains by cross correlation between two images. Thus, the frame rate is of high importance for a proper DIC analysis. In contrast, IRT directly measures the temperature for each individual image/deformation state without the need of the information from earlier states. Therefore, the right frame rate is less important for an analysis by IRT than for DIC.

The correlation of DIC and IRT in a fully-coupled thermomechanical analysis using not only the primary variables strain and temperature but also their corresponding rates in form of local field images and line plots allows for a deep insight in the mesomechanical deformation of stochastic as well as periodic cellular materials. Although DIC only provides surface information, it is able to capture the entire local deformation history of a material such as the evolution of strain bands. The line plots can be used to determine the location and the width of deformation bands. The use of the local strain rate fields and the corresponding line plots allows for the analysis of the current deformation zones in the material, similar to the information provided by the direct temperature measurement of IRT. Nevertheless, IRT provides at least partial information of the deformation behavior in the specimen volume and not only on the surface, especially for cellular materials. But a meaningful IRT analysis needs sufficient heat production during the deformation. The local temperature rate fields are very reliable to visualize locations of current deformation also in the volume. Nevertheless, heat loss due to convection and conduction can be a big problem in IRT analysis leading to diffuse broad deformation zones, while DIC provides narrow deformation zones. Hence, both methods have their advantages and disadvantages, but a correlative use of DIC and IRT is beneficial for studying local deformation mechanism in cellular materials as well as bulk materials.

ACKNOWLEDGEMENTS

We kindly acknowledge the ARALON COLOR GmbH for providing the luminescent pigments. We would also like to thank Michael Fries for preparing the polymer templates of the auxetic structures. Open Access funding enabled and organized by Projekt DEAL.

CONFLICT OF INTEREST

The authors declare no potential conflict of interests.

REFERENCES

[1] M. Adorna, S. Brodner, J. Falta, P. Zlámal, and T. Fíla, Evaluation of hopkinson bar experiments using multiple digital image correlation software tools, Acta Polytechn. CTU Proc. **25** (2019), 1–5.

[2] K. L. Alderson, How to make auxetic fibre reinforced composites, Phys. Status Solidi B **242** (2009), no. 3, 509–518.

[3] H. Bart-Smith, A. F. Bastawros, D. R. Mumm, A. G. Evans, D. J. Sypeck, and H. N. G. Wadley, Compressive deformation and yielding mechanisms in cellular al alloys determined using x-ray tomography and surface strain mapping, MRS Online Proc. Lib (OPL) **521** (1998), 71–81.

[4] A. Bastawros, H. Bart-Smith, and A. Evans, Experimental analysis of deformation mechanisms in a closed-cell aluminum alloy foam, J. Mech. Phys. Solids **48** (2000), no. 2, 301–322.

[5] A. Bastawros and A. Evans, "*Deformation heterogeneity in cellular al alloys revealed by surface deformation analysis*," *Metal foams and porous metal structures*, MIT, Bremen, 1999, pp. 221–226.

[6] A. Bastawros and R. McManuis, Case study: Use of digital image analysis software to measure non-uniform deformation in cellular aluminum alloys, Comput. Stand. Interfaces **6** (1999), no. 20, 459–460.

[7] A. Bezazi and F. Scarpa, Mechanical behaviour of conventional and negative poisson's ratio thermoplastic polyurethane foams under compressive cyclic loading, Int. J. Fatigue **29** (2007), no. 5, 922–930.

15222608, 2022, 3-4, Downloaded from https://onlinelibrary.wiley.com/doi/10.1002/gamm.202200014 by Universitaet Des Saarlandes, Wiley Online Library on [18/10/2022]. See the Terms and Conditions (https://onlinelibrary.wiley.com/terms-and-conditions) on Wiley Online Library for rules of use; OA articles are governed by the applicable Creative Commons License

[8] Y. Boonyongmaneerat, C. A. Schuh, and D. C. Dunand, Mechanical properties of reticulated aluminum foams with electrodeposited NI–W coatings, Scr. Mater. **59** (2008), no. 3, 336–339.

[9] B. Bouwhuis, M. C. JL, G. Palumbo, and G. D. Hibbard, Mechanical properties of hybrid nanocrystalline metal foams, Acta Mater. **57** (2009), no. 14, 4046–4053.

[10] O. Breitenstein, *Lock-in infrared thermography for ic failure analysis*, Proc. 36th Int. Symp. Test. Failure Anal.

[11] S. Bronder, S. Diebels, and A. Jung, Neural networks for structural optimisation of mechanical metamaterials, PAMM **20** (2021), no. 1, e202000238.

[12] S. Bronder, F. Herter, A. Röhrig, D. Bähre, and A. Jung, Design study for multifunctional 3D-reentrant auxetics, Adv. Eng. Mater. **24** (2021), 2100816.

[13] S. Bronder, M. Adorna, T. Fíla, P. Koudelka, J. Falta, O. Jiroušek, and A. Jung, Hybrid auxetic structures: Structural optimization and mechanical characterization, Adv. Eng. Mater. **2001393** (2021), 2001393.

[14] S. Broxtermann, M. Vesenjak, L. Krstulović-Opara, and T. Fiedler, Quasi static and dynamic compression of zinc syntactic foams, J. Alloys Compd. **768** (2018), 962–969. https://doi.org/10.1016/j.jallcom.2018.07.215.

[15] N. Cholewa, P. T. Summers, S. Feih, A. P. Mouritz, B. Y. Lattimer, and S. W. Case, A technique for coupled thermomechanical response measurement using infrared thermography and digital image correlation (TDIC), Exp. Mech. **56** (2016), no. 2, 145–164.

[16] A. Chrysafi, N. Athanasopoulos, and N. Siakavellas, Damage detection on composite materials with active thermography and digital image processing, Int. J. Therm. Sci. **116** (2017), 242–253.

[17] A. Chrysochoos, V. Huon, F. Jourdan, J. M. Muracciole, R. Peyroux, and B. Wattrisse, Use of full-field digital image correlation and infrared thermography measurements for the thermomechanical analysis of material behaviour, Strain **46** (2010), no. 1, 117–130.

[18] T. Chu, W. Ranson, and M. A. Sutton, Applications of digital-image-correlation techniques to experimental mechanics, Exp. Mech. **25** (1985), no. 3, 232–244.

[19] S. H. Daly, "*Digital image correlation in experimental mechanics for aerospace materials and structures*," *Encyclopedia of aerospace engineering*, John Wiley & Sons, Ltd., Hoboken, NJ 2010, pp. 1–12. https://doi.org/10.1002/9780470686652.eae542.

[20] M. Dolce and D. Cardone, Mechanical behaviour of shape memory alloys for seismic applications 1. Martensite and austenite NiTi bars subjected to torsion, Int. J. Mech. Sci. **43** (2001), no. 11, 2631–2656. https://doi.org/10.1016/S0020-7403(01)00049-2.

[21] Y. Dong and B. Pan, A review of speckle pattern fabrication and assessment for digital image correlation, Exp. Mech. **57** (2017), no. 8, 1161–1181. https://doi.org/10.1007/s11340-017-0283-1.

[22] I. Duarte, M. Vesenjak, and L. Krstulović-Opara, Compressive behaviour of unconstrained and constrained integral-skin closed-cell aluminium foam, Compos. Struct. **154** (2016), 231–238.

[23] I. Duarte, M. Vesenjak, L. Krstulović-Opara, and Z. Ren, Crush performance of multifunctional hybrid foams based on an aluminium alloy open-cell foam skeleton, Polym. Test. **67** (2018), 246–256. https://doi.org/10.1016/j.polymertesting.2018.03.009.

[24] I. Duarte, N. Peixinho, A. Andrade-Campos, and R. Valente, Special issue on cellular materials, Sci. Technol. Mater. **30** (2018), no. 1, 1–3. https://doi.org/10.1016/j.stmat.2018.05.001.

[25] I. Duarte, T. Fiedler, L. Krstulović-Opara, and M. Vesenjak, Brief review on experimental and computational techniques for characterization of cellular metals, Metals **10** (2020), no. 6, 243–261.

[26] K. K. Dudek, W. Wolak, R. Gatt, and J. N. Grima, Impact resistance of composite magnetic metamaterials, Sci. Rep. **9** (2019), no. 1, 1–9.

[27] T. Fíla, I. Kumpová, P. Koudelka, P. Zlámal, D. Vavřík, O. Jiroušek, and A. Jung, Dual-energy x-ray micro-ct imaging of hybrid ni/al open-cell foam, J. Instrum. **11** (2016), no. 01, C01005.

[28] S. F. Fischer, Energy absorption efficiency of open-cell pure aluminum foams, Mater. Lett. **184** (2016), 208–210.

[29] M. Frey, T. Romero, A. C. Roger, and D. Edouard, Open cell foam catalysts for co2 methanation: Presentation of coating procedures and in situ exothermicity reaction study by infrared thermography, Catal. Today **273** (2016), 83–90.

[30] T. Fíla, P. Koudelka, J. Falta, P. Zlámal, V. Rada, M. Adorna, S. Bronder, and O. Jiroušek, Dynamic impact testing of cellular solids and lattice structures: Application of two-sided direct impact hopkinson bar, Int. J. Impact Eng. **148**, (2020), 103767. http://www.sciencedirect.com/science/article/pii/S0734743X2030837X.

[31] C. Grill, M. Fries, A. Jung, and S. Diebels, Numerical and experimental investigations of the electrodeposition process on open porous foams, determination of the parameter influence on the coating homogeneity, Int. J. Heat Mass Transf. **180** (2021), 121791.

[32] O. Jiroušek, T. Doktor, D. Kytýř, P. Zlámal, T. Fíla, P. Koudelka, I. Jandejsek, and D. Vavřík, X-ray and finite element analysis of deformation response of closed-cell metal foam subjected to compressive loading, J. Instr. **8** (2013), no. 02, C02012.

[33] A. Jung and S. Diebels, Synthesis and mechanical properties of novel Ni/PU hybrid foams: A new economic composite material for energy absorbers, Adv. Eng. Mater. **18** (2016), no. 4, 532–541.

[34] A. Jung and S. Diebels, Microstructural characterisation and experimental determination of a multiaxial yield surface for open-cell aluminium foams, Mater. Des. **131** (2017), 252–264.

[35] A. Jung and S. Diebels, Yield surfaces for solid foams: A review on experimental characterization and modeling, GAMM-Mitteilungen **41** (2018), no. 2, e201800002.

[36] A. Jung, H. Natter, R. Hempelmann, S. Diebels, M. R. Koblischka, U. Hartmann, and E. Lach, Electrodeposition of nanocrystalline metals on open cell metal foams: Improved mechanical properties, ECS Trans. **25** (2010), no. 41, 165–172.

[37] A. Jung, H. Natter, S. Diebels, E. Lach, and R. Hempelmann, Nanonickel coated aluminum foam for enhanced impact energy absorption, Adv. Eng. Mater. **13** (2011), no. 1–2, 23–28.

[38] A. Jung, S. Diebels, A. Koblischka-Veneva, J. Schmauch, A. Barnoush, and M. R. Koblischka, Microstructural analysis of electrochemical coated open-cell metal foams by ebsd and nanoindentation, Adv. Eng. Mater. **16** (2014), no. 1, 15–20.

15222608, 2022, 3-4, Downloaded from https://onlinelibrary.wiley.com/doi/10.1002/gamm.202200014 by Universitaet Des Saarlandes, Wiley Online Library on [18/10/2022]. See the Terms and Conditions (https://onlinelibrary.wiley.com/terms-and-conditions) on Wiley Online Library for rules of use; OA articles are governed by the applicable Creative Commons License

[39] A. Jung, Z. Chen, J. Schmauch, C. Motz, and S. Diebels, Micromechanical characterisation of ni/al hybrid foams by nano-and microindentation coupled with ebsd, Acta Mater. **102** (2016), 38–48.

[40] A. Jung, J. Luksch, S. Diebels, F. Schäfer, and C. Motz, In-situ and ex-situ microtensile testing of individual struts of al foams and ni/al hybrid foams, Mater. Des. **153** (2018), 104–119.

[41] A. Jung, S. Bronder, S. Diebels, M. Schmidt, and S. Seelecke, Thermographic investigation of strain rate effects in al foams and ni/al hybrid foams, Mater. Des. **160** (2018), 363–370.

[42] A. Jung, K. al Majthoub, C. Jochum, S. M. Kirsch, F. Welsch, S. Seelecke, and S. Diebels, Correlative digital image correlation and infrared thermography measurements for the investigation of the mesoscopic deformation behaviour of foams, J. Mech. Phys. Solids **130** (2019), 165–180.

[43] S.-M. Kirsch, F. Welsch, N. Michaelis, M. Schmidt, A. Wieczorek, J. Frenzel, G. Eggeler, A. Schütze, and S. Seelecke, NiTi-based Elastocaloric cooling on the macroscale: From basic concepts to realization, Energy Technol. **6** (2018), no. 8, 1567–1587. https://doi.org/10.1002/ente.201800152.

[44] K. König, M. Reis, and A. Jung, *Application of ultraviolet (uv) radiation and fluorescence for dic measurements - quality improvement*, submitted, 2021.

[45] L. Krstulović-Opara, M. Surjak, M. Vesenjak, Z. Tonković, J. Kodvanj, and Ž. Domazet, Comparison of infrared and 3d digital image correlation techniques applied for mechanical testing of materials, Infrared Phys. Technol. **73** (2015), 166–174.

[46] L. Krstulović-Opara, M. Vesenjak, I. Duarte, Z. Ren, and Ž. Domazet, Infrared thermography as a method for energy absorption evaluation of metal foams, Mater Today Proc **3** (2016), no. 4, 1025–1030.

[47] R. Lakes, Foam structures with a negative poisson's ratio, Science **235** (1987), 1038–1040.

[48] R. Lakes, Design considerations for materials with negative poisson's ratios, J. Mech. Des. **115** (1993), no. 4, 696–700.

[49] R. S. Lakes, Negative-poisson's-ratio materials: Auxetic solids, Annu. Rev. Mater. Res. **47** (2017), 63–81.

[50] T.-C. Lim, *Mechanics of metamaterials with negative parameters*, Springer Nature, Singapore, 2020.

[51] X. Maldague, Applications of infrared thermography in nondestructive evaluation, Trends Opt. Nondestruct. Test. (2000), 591–609.

[52] X. P. Maldague, *Nondestructive evaluation of materials by infrared thermography*, Springer-Verlag, London, 2012.

[53] A. Mauko, T. Fíla, J. Falta, P. Koudelka, V. Rada, M. Neuhäuserová, P. Zlámal, M. Vesenjak, O. Jiroušek, and Z. Ren, Dynamic deformation behaviour of chiral auxetic lattices at low and high strain-rates, Metals **11** (2021), no. 1, 52.

[54] C. Meola and G. M. Carlomagno, Recent advances in the use of infrared thermography, Measur. Sci. Technol. **15** (2004), no. 9, R27.

[55] N. Michaelis, F. Welsch, S. M. Kirsch, M. Schmidt, S. Seelecke, and A. Schütze, Experimental parameter identification for elastocaloric air cooling, Int. J. Refrig. **100** (2019), 167–174. https://doi.org/10.1016/j.ijrefrig.2019.01.006. https://linkinghub.elsevier.com/retrieve/pii/S0140700719300064.

[56] N. Michaelis, A. Schütze, F. Welsch, S. M. Kirsch, and S. Seelecke, Novel experimental approach to determine Elastocaloric latent heat, Shape Memory Superelast. **5** (2019), no. 4, 352–361. https://doi.org/10.1007/s40830-019-00249-y. http://link.springer.com/10.1007/s40830-020-00265-3.

[57] N. Novak, M. Vesenjak, and Z. Ren, Crush behaviour of auxetic cellular structures, Sci. Technol. Mater. **30** (2018), no. 1, 4–7.

[58] N. Novak, Blast response study of the sandwich composite panels with 3d chiral auxetic core, Compos. Struct. **210** (2019), 167–178. http://www.sciencedirect.com/science/article/pii/S0263822318336845.

[59] N. Novak, M. Vesenjak, S. Tanaka, K. Hokamoto, and Z. Ren, Compressive behaviour of chiral auxetic cellular structures at different strain rates, Int. J. Impact Eng. **103566** (2020), 103566.

[60] R. A. Osornio-Rios, J. A. Antonino-Daviu, and R. de Jesus Romero-Troncoso, Recent industrial applications of infrared thermography: A review, IEEE Trans. Ind. Inform. **15** (2018), no. 2, 615–625.

[61] B. Pan, K. Qian, H. Xie, and A. Asundi, Two-dimensional digital image correlation for in-plane displacement and strain measurement: A review, Meas. Sci. Technol. **20** (2009), no. 6, 062001.

[62] A. Pehilj, The detection of plastic flow propagation based on the temperature gradient, Mater. Today Proc. **4** (2017), no. 5, 5925–5930.

[63] S. C. Pinto, P. A. A. P. Marques, M. Vesenjak, R. Vicente, L. Godinho, L. Krstulović-Opara, and I. Duarte, Characterization and physical properties of aluminium foam–Polydimethylsiloxane nanocomposite hybrid structures, Compos. Struct. **230** (2019), 111521. https://doi.org/10.1016/j.compstruct.2019.111521.

[64] R. Prakash, Infrared thermography, InTech, Rijeka, Croatia (2012).

[65] B. Reedlunn, Tips and tricks for characterizing shape memory wire part 5: Full-field strain measurement by digital image correlation, Exp. Tech. **37** (2013), no. 3, 62–78. https://deepblue.lib.umich.edu/bitstream/handle/2027.42/98220%/ext717.pdf?sequence=1{&}isAllowed=y http://doi.wiley.com/10.1111/j.1747-1567.2011.00717.x.

[66] F. Scarpa, P. Pastorino, A. Garelli, S. Patsias, and M. Ruzzene, Auxetic compliant flexible pu foams: Static and dynamic properties, Phys. Status Solidi B **242** (2005), no. 3, 681–694.

[67] T. A. Schaedler and W. B. Carter, Architected cellular materials, Annu. Rev. Mater. Res. **46** (2016), no. 1, 187–210.

[68] M. Schmidt, J. Ullrich, A. Wieczorek, J. Frenzel, G. Eggeler, A. Schütze, and S. Seelecke, Experimental methods for investigation of shape memory based elastocaloric cooling processes and model validation, J. Vis. Exp. (2016), no. 111, e53626. http://www.jove.com/video/53626/experimental-methods-for-investigation-shape-memory-based.

[69] A. Sendrowicz, Challenges and accomplishments in mechanical testing instrumented by in situ techniques: Infrared thermographydigital image correlation, and acoustic emission, Appl. Sci. (Switzerland) **11** (2021), no. 15, 1–38.

15222608, 2022, 3-4, Downloaded from https://onlinelibrary.wiley.com/doi/10.1002/gamm.202200014 by Universitaet Des Saarlandes, Wiley Online Library on [18/10/2022]. See the Terms and Conditions (https://onlinelibrary.wiley.com/terms-and-conditions) on Wiley Online Library for rules of use; OA articles are governed by the applicable Creative Commons License

[70] J. Shaw and S. Kyriakides, On the nucleation and propagation of phase transformation fronts in a NiTi alloy, Acta Mater. **45** (1997), no. 2, 683–700. https://www.sciencedirect.com/science/article/abs/pii/S135964%5496001899?via{%}3Dihub https://linkinghub.elsevier.com/retrieve/pii/S1359645496001899.
[71] E. Solórzano, F. Garcia-Moreno, N. Babcsán, and J. Banhart, Thermographic monitoring of aluminium foaming process, J. Nondestruct. Eval. **28** (2009), no. 3–4, 141–148.
[72] Y. Sun, R. Burgueño, W. Wang, and I. Lee, Modeling and simulation of the quasi-static compressive behavior of al/cu hybrid open-cell foams, Int. J. Solids Struct. **54** (2015), 135–146.
[73] M. Sutton, Full-field representation of discretely sampled surface deformation for displacement and strain analysis, Exp. Mech. **31** (1991), no. 2, 168–177.
[74] P. Thornton and C. Magee, The deformation of aluminum foams, Metall. Trans. A. **6** (1975), no. 6, 1253–1263.
[75] D. Tomažinčič, Predicting the fatigue life of an alsi9cu3 porous alloy using a vector-segmentation technique for a geometric parameterisation of the macro pores, Metals **11** (2021), no. 1, 1–21.
[76] E. Verhulp, B. van Rietbergen, and R. Huiskes, A three-dimensional digital image correlation technique for strain measurements in microstructures, J. Biomech. **37** (2004), no. 9, 1313–1320.
[77] M. Vesenjak, K. Hokamoto, M. Sakamoto, T. Nishi, L. Krstulović-Opara, and Z. Ren, Mechanical and microstructural analysis of unidirectional porous (UniPore) copper, Mater. Des. **90** (2016), 867–880.
[78] M. Vollmer and K.-P. Möllmann, *Infrared thermal imaging: Fundamentals, research and applications*, John Wiley & Sons, Weinheim, Germany 2017.
[79] F. Welsch, J. Ullrich, H. Ossmer, M. Schmidt, M. Kohl, C. Chluba, E. Quandt, A. Schütze, and S. Seelecke, Numerical simulation and experimental investigation of the elastocaloric cooling effect in sputter-deposited TiNiCuCo thin films, Contin. Mech. Thermodyn. **30** (2018), no. 1, 53–68. https://doi.org/10.1007/s00161-017-0582-x.
[80] J. Zhou, P. Shrotriya, and W. Soboyejo, Mechanisms and mechanics of compressive deformation in open-cell al foams, Mech. Mater. **36** (2004), no. 8, 781–797.
[81] J. Zhou, Z. Gao, A. M. Cuitino, and W. O. Soboyejo, Effects of heat treatment on the compressive deformation behavior of open cell aluminum foams, Mater. Sci. Eng. A **386** (2004), no. 1–2, 118–128.

How to cite this article: S. Grednev, S. Bronder, F. Kunz, M. Reis, S. -M. Kirsch, F. Welsch, S. Seelecke, S. Diebels, and A. Jung, *Applicability of correlated digital image correlation and infrared thermography for measuring mesomechanical deformation in foams and auxetics*, GAMM-Mitteilungen. **45** (2022), e202200014. https://doi.org/10.1002/gamm.202200014

15222608, 2022, 3-4, Downloaded from https://onlinelibrary.wiley.com/doi/10.1002/gamm.202200014 by Universitaet Des Saarlandes, Wiley Online Library on [18/10/2022]. See the Terms and Conditions (https://onlinelibrary.wiley.com/terms-and-conditions) on Wiley Online Library for rules of use; OA articles are governed by the applicable Creative Commons License